Ground-based contrail observations: comparisons with flight telemetry and contrail model estimates

Jade Low[1], Roger Teoh[1], Joel Ponsonby[1], Edward Gryspeerdt[2], Marc Shapiro[3], and Marc E.J. Stettler[1]

[1]Department of Civil and Environmental Engineering, Imperial College London, London, SW7 2AZ, United Kingdom
[2]Grantham Institute for Climate Change and the Environment, Imperial College London, London, SW7 2AZ, United Kingdom
[3]Breakthrough Energy, 4110 Carillon Point, Kirkland, WA 98033, United States

Correspondence to: Marc E.J. Stettler (m.stettler@imperial.ac.uk)

Abstract. Observations of contrails are vital for improving understanding of contrail formation and lifecycle, informing models, and assessing contrail mitigation strategies. Ground-based cameras offer a cost-effective means to observe the formation and evolution of young contrails and can be used to assess the accuracy of existing models. Here, we develop a methodology to track and analyse contrails from ground-based cameras, comparing these observations against simulations from the contrail cirrus prediction model (CoCiP) with actual flight trajectories. The ground-based contrail observations consist of 14 h of video footage recorded on five different days over Central London, capturing a total of 1,619 flight waypoints from 283 unique flights. Our results suggest that the best agreement between the observed and simulated contrail formation occurs at around 35,000–40,000 feet and at temperatures at least 10 K below the Schmidt-Appleman Criterion threshold temperature (T_{SAC}). Conversely, the largest discrepancies occurred when contrails are formed below 30,000 feet and at temperatures within 2.5 K of T_{SAC}. On average, the simulated contrail width is 17.5% smaller than the observed geometric width. This discrepancy could be caused by the underestimation of sub-grid scale wind shear and turbulent mixing in the simulation, and model representation of the contrail cross-sectional shape. Overall, these findings demonstrate the capability of ground-based cameras to inform weather and contrail model development when combined with flight telemetry.

1 Introduction

Contrails, line-shaped clouds that form behind an aircraft at altitudes of 8–13 km, occur when conditions in the exhaust plume fulfil the Schmidt-Appleman Criterion (SAC) (Schumann, 1996). Under these conditions, the relative humidity (RH) in the exhaust plume reaches liquid saturation causing water vapour to condense onto the surface of soot particles, which subsequently freeze to form contrail ice crystals. These newly formed contrail ice particles are entrained in the aircraft's wake vortices, and in most cases, contrails that are formed disappear within a few minutes as adiabatic heating causes the ice particles to sublimate (Lewellen and Lewellen, 2001; Unterstrasser, 2016). However, a small fraction of contrails can persist beyond a few minutes when the atmosphere is ice supersaturated, i.e., relative humidity with respect to ice (RHi) exceeding 100% (Jensen et al., 1998). According to the definition provided by the World Meteorological Organization (2017), contrails that

survive for at least 10 minutes are known as persistent contrails. Over time, persistent contrails tend to spread and mix with other contrails and natural clouds to form contrail cirrus clusters (Haywood et al., 2009) affecting the Earth's radiative balance and producing a net warming effect (Meerkötter et al., 1999; Fuglestvedt et al., 2010). Recent studies suggests that the global annual mean contrail cirrus net radiative forcing (RF) in 2019 (62.1 [34.8, 74.8] mW m^{-2}) (Quaas et al., 2021; Teoh et al.,

35 2023) could be around two times greater than the RF from aviation's cumulative CO_2 emissions (34.3 [31, 38] mW m^{-2}) (Lee et al., 2021).

Different modelling approaches are available to simulate the contrail properties and climate forcing, including: (i) large-eddy simulations (LES) (Unterstrasser, 2016; Lewellen et al., 2014; Lewellen, 2014); (ii) general circulation models (GCM) (Chen and Gettelman, 2013; Bier and Burkhardt, 2022); (iii) Lagrangian models based on parameterised physics, such as the contrail

40 cirrus prediction model (CoCiP) (Schumann, 2012); and (iv) climate change functions (CCFs) and algorithmic climate change functions (aCCFs) (Grewe et al., 2014; Dietmüller et al., 2023). These contrail modelling approaches have been used to estimate the global and regional contrail climate forcing (Chen and Gettelman, 2013; Bock and Burkhardt, 2016; Schumann et al., 2021; Bier and Burkhardt, 2022; Teoh et al., 2023) and explore the effectiveness of different mitigation strategies (Teoh et al., 2020b, 2022b; Schumann et al., 2011; Grewe et al., 2017; Burkhardt et al., 2018; Caiazzo et al., 2017).

45 To enhance confidence and ensure that any proposed contrail mitigation solution yields a net climate benefit, it is crucial that contrail model outputs are extensively validated against measurements and observations. Existing studies have compared the simulated contrail properties from CoCiP relative to in-situ measurements, remote sensing, and satellite observations, where the results generally show a good agreement between the measured and simulated contrail properties at various stages of their lifecycle (Schumann et al., 2017, 2021; Teoh et al., 2023). However, these comparisons were conducted on an aggregate level,

50 focusing on an ensemble of contrails, and thus do not provide insights into the evaluation of individual contrails formed by unique flights. While Jeßberger et al. (2013) has assessed the simulated contrail properties from CoCiP with in-situ measurements of young contrails formed by different passenger aircraft types, these measurements were made at a single point in time and the study remains limited to three data points. Satellite observations, on the other hand, can partially address some of these limitations by enabling a large number of contrails to be measured, matched with specific flights and tracked over

55 time (Vázquez-Navarro et al., 2015; Tesche et al., 2016; Duda et al., 2019; Marjani et al., 2022; Gryspeerdt et al., 2023), but it remains challenging for satellites to detect young contrails with sub-pixel width, aged contrail cirrus, cases with cloud-contrail overlap, and contrails with small optical depth (< 0.05) (Mannstein et al., 2010; Kärcher et al., 2010; Meijer et al., 2022).

Ground-based instruments, such as lidar and cameras, can be used in tandem with in-situ measurements and satellite

60 observations in the validation of contrail models (Mannstein et al., 2010; Schumann et al., 2013; Rosenow et al., 2023). In particular, contrail observations from ground-based cameras can address some of the satellite limitations because they can be set up at a lower relative cost, are effective in observing the formation and evolution of young contrails at very high temporal and spatial resolutions, and are capable of detecting optically thin contrails (Mannstein et al., 2010). However, previous research that utilised ground-based instruments predominantly focused on natural cirrus observations (Long et al., 2006; Feister

65   et al., 2010; Seiz et al., 2007), and two small-scale studies have compared a total of 16 observed contrail properties (3D position, width, and/or persistence) with model estimates (Schumann et al., 2013; Rosenow et al., 2023). Recognising the potential of ground-based cameras, this study aims to: (i) develop an algorithm to detect and analyse contrails that are observed by ground-based cameras; and (ii) extend the use of camera observations to evaluate the simulated contrail outputs from the CoCiP contrail model on a larger-scale compared to prior studies.

2 Materials and methods

This section describes the contrail observations that were captured by the ground-based camera (Section 2.1), the workflow that is used to simulate the formation and evolution of contrails (Section 2.2), and the methods used to superimpose the actual flight trajectories and simulated contrails onto the video footage (Section 2.3) and to compare between the observed and simulated contrails properties (Section 2.4). Fig. 1 provides an overview of the step-by-step process and datasets used to compare the ground-based contrail observations with the simulated contrail outputs.
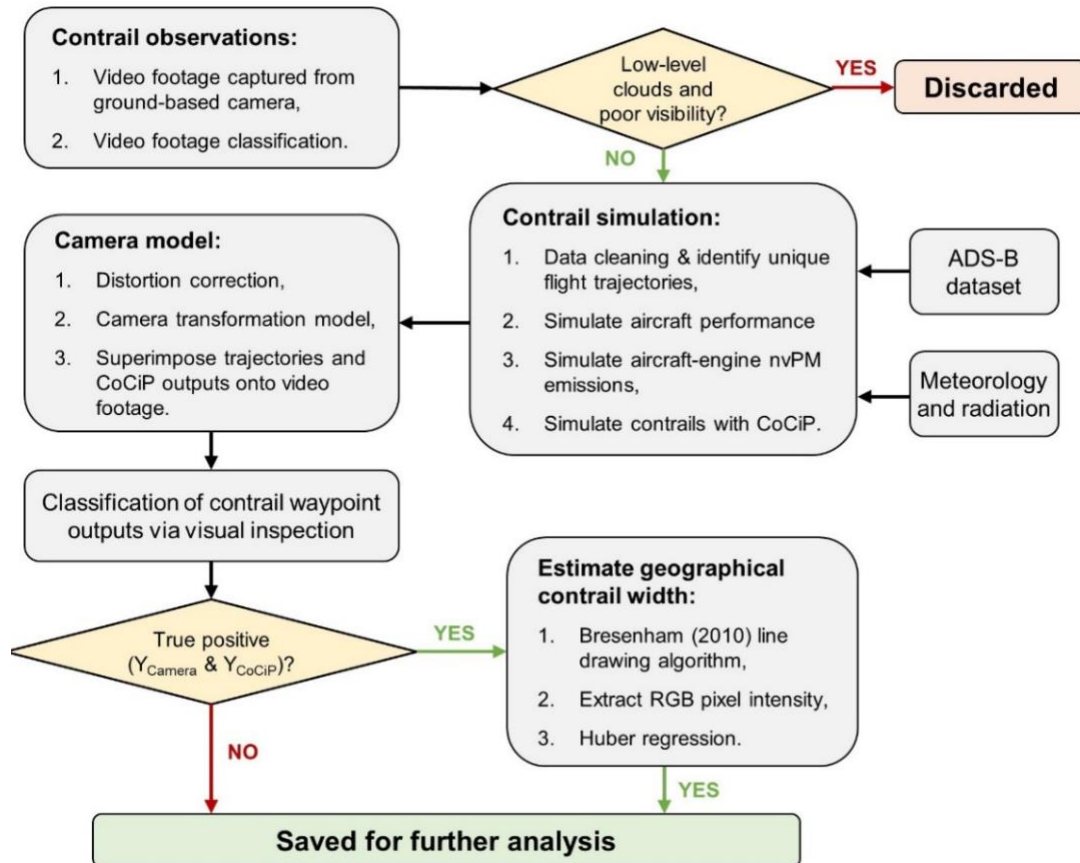
Figure 1: Overview of the step-by-step process and datasets used to compare the ground-based contrail observations with the simulated contrail outputs from CoCiP.

2.1 Contrail observations

80   Contrail observations were made using a Raspberry Pi Camera Module v2.1 which features an 8 Megapixel sensor (3280 x 2464 pixels), a wide-angle field of view spanning 62.2° horizontally and 48.8° vertically, and a focal length of 3.04 mm (Raspberry Pi, n.d.). The camera was positioned at Imperial College London's South Kensington Campus (51.4988°N, 0.1788°W) at an elevation of 25 m and pitched at a 25° angle above the horizontal plane. Recordings were taken between October-2021 and April-2022 during daylight hours, and at a temporal resolution of 5 seconds per frame. The captured footage

85   is then filtered to remove the time intervals with low-level clouds and poor visibility (i.e., nighttime and periods with significant glare from direct sunlight) (Appendix A1). This filtering results in a final dataset containing 14 h of video footage collected over 5 different days, and 283 unique flights were observed during these specific time frames.

2.2 Contrail simulation

The formation and evolution of contrails that were observed by the video footage are simulated using CoCiP (Schumann,

90   2012), a contrail model that can now be accessed via the pycontrails repository on GitHub (Shapiro et al., 2023). Several datasets and methods are required as inputs to CoCiP, including the: (i) actual flight trajectories; (ii) historical meteorology and radiation fields; and (iii) aircraft performance and emissions estimates.

2.2.1 Flight trajectories

The trajectories for each flight were derived using the raw Automatic Dependent Surveillance – Broadcast (ADS-B) telemetry

95   that was purchased from Spire Aviation (Teoh et al., 2024). Each ADS-B waypoint contains the unique flight identifier (call sign and flight number) and its corresponding 4D position (longitude, latitude, barometric altitude, and time) provided at time intervals of 40 s, and we filter the dataset to only include waypoints that were broadcasted within a defined spatial bounding box (10°W, 40°N, 10°E, 60°N) that extends approximately ±10° in longitude and latitude from camera's location.

2.2.2 Meteorology

100   The historical 4D meteorological fields within the defined spatial bounding box (between 40 – 60° N and 10° W – 10° E) were provided by the European Centre for Medium Range Weather Forecast (ECMWF) ERA5 high-resolution realisation (HRES) reanalysis (ECMWF, 2021; Hersbach et al., 2020) at a spatial resolution of 0.25° longitude × 0.25° latitude over 37 pressure levels and at a 1 h temporal resolution. We note that corrections were applied to the ERA5 HRES humidity fields (Teoh et al., 2022a) to ensure that the RHi distribution is consistent with in-situ measurements from the In-service Aircraft for a Global

105   Observing System (IAGOS) dataset (Petzold et al., 2015; Boulanger et al., 2022). For each flight waypoint, the local meteorology is estimated from a quadrilinear interpolation across the three space coordinates and time (Schumann, 2012).

2.2.3 Aircraft performance and nvPM emissions

The interpolated temperature and wind vectors are used to estimate the Mach number at each flight waypoint. These meteorological variables are then used as inputs to the Base of Aircraft Data Family 4.2 (BADA 4) aircraft performance model to estimate the: (i) fuel mass flow rate; (ii) change in aircraft mass, assuming that the initial aircraft mass at the first known waypoint is equal to the nominal (reference) mass that is provided by BADA; (iii) overall efficiency; and (iv) engine thrust settings (EUROCONTROL, 2016). We then estimate the aircraft-engine specific non-volatile particulate matter (nvPM) number emissions index (EI_n) according to Teoh et al. (2022a), which utilises the T_4/T_2 methodology when the nvPM emissions profile for the specific aircraft-engine type is covered in the ICAO Aircraft Engine Emissions Databank (EDB) (EASA, 2021) or the fractal aggregates (FA) model if the engine-specific nvPM data is not available (Teoh et al., 2020b). All flights are assumed to be powered by conventional Jet A-1 fuel.

2.2.4 Contrail cirrus prediction model

CoCiP assumes that contrails form when the ambient temperature (T_{amb}) at the flight waypoint is below the SAC threshold temperature (T_{SAC}), and two successive waypoints that satisfy the SAC forms a contrail segment (Schumann, 2012). A parametric wake vortex model is then used to simulate the wake vortex downwash (Holzapfel, 2003), and persistent contrails are defined when their post-wake vortex ice water content (IWC) remains above 10^{-12} kg kg^{-1}. The evolution of these persistent contrail segments is then simulated using a Runge-Kutta scheme with the model time step (dt) of 40 s until the ice particle number concentration or optical depth drops below 10^3 m^{-3} and 10^{-6}, respectively, or when the mid-point of the contrail plume advects beyond the domain of interest (40 – 60° N and 10° W – 10° E). We specifically selected a dt that is significantly smaller than the typical range that was used in previous studies (1800–3600 s) (Schumann et al., 2015; Teoh et al., 2020a, 2022a) to superimpose the simulated contrail outputs to the video footage and perform a more comprehensive assessment of the early-stage contrail evolution.

2.3 Camera transformation model

Before comparing the camera observations with aircraft positions and simulated CoCiP outputs, we first correct any radial and tangential distortion of the video footage using the OpenCV homography method (Bradski, 2000), specifically applying the chessboard calibration technique (Tsai, 1987; Wu et al., 2015) described in Appendix A2. After correcting for distortions, we project the simulated contrail waypoints and dimensions onto the video footage using a camera transformation model which follows a two-step process: (i) the real-world 3D positions (i.e., ADS-B flight waypoints and the simulated mid-point and edges of the contrail plumes) are mapped to a 3D camera coordinate system (X, Y, Z) using an extrinsic (rotation) matrix; followed by (ii) transforming the 3D camera coordinates (X, Y, Z) to a 2D pixel coordinate system (u, v) using an intrinsic (camera) matrix. Further details of the camera transformation model can be found in Appendix A3. Figure 2 provides an example of the superimposed flight trajectories and simulated contrail properties to the video footage at time intervals of 40 s.
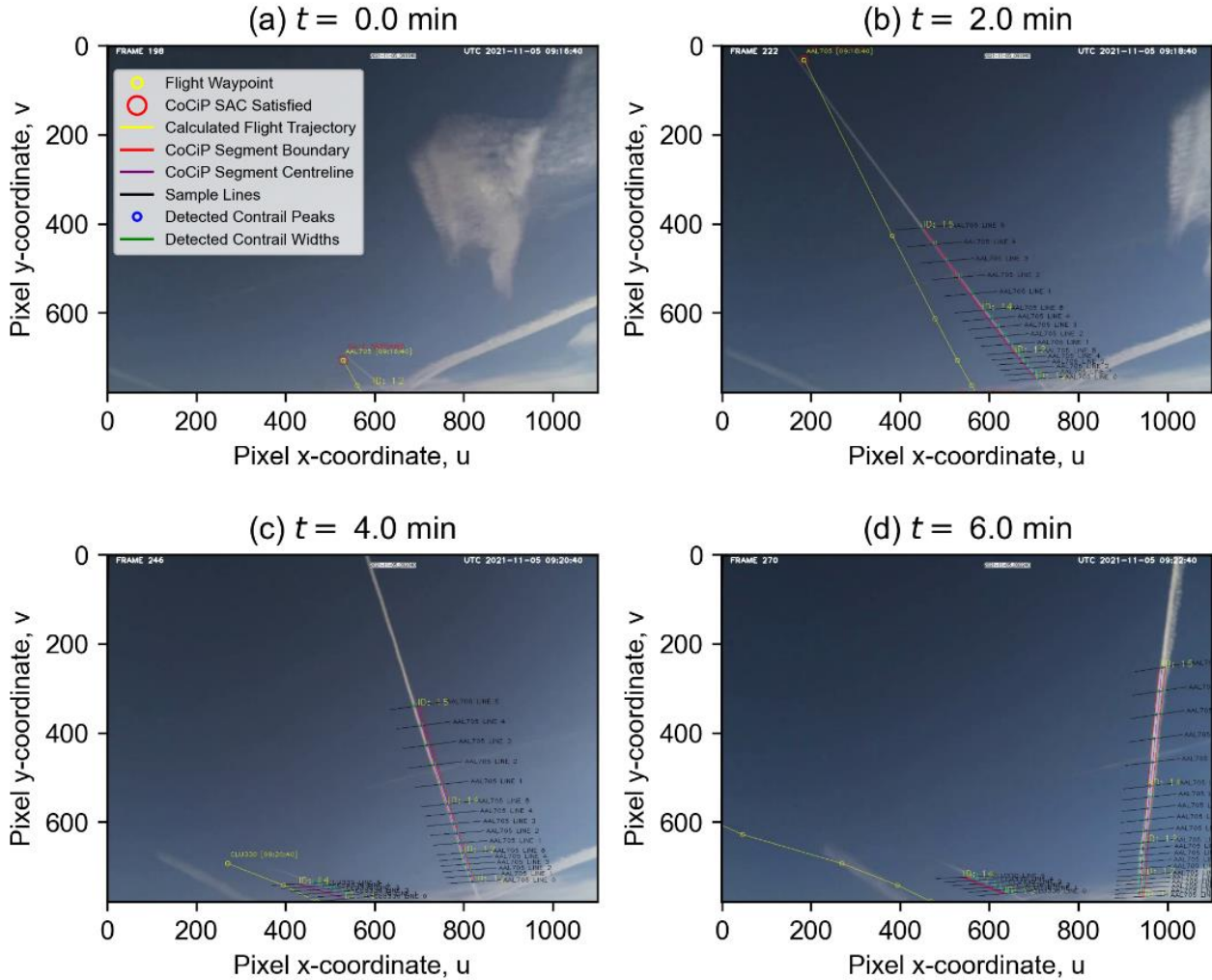
Figure 2: Example of the flight trajectories and simulated contrail properties from CoCiP that are superimposed to the video footage using the camera transformation model, c.f. Eq. (1) and Eq. (2). The flight trajectories and contrails were observed on 5-Nov-2021 between 09:16:40 and 09:22:40 (UTC).

2.4 Comparison between contrail observation and simulation

We visually compare the simulated contrail formation with observations and classify each ADS-B waypoint into four groups to quantify the probability of: (i) true positive cases, $P(Y_{Camera} \& Y_{CoCiP})$, where the contrail formed at that waypoint is observed by the camera (Y_{Camera}) and predicted in the simulation (Y_{CoCiP}), i.e., SAC is fulfilled in CoCiP; (ii) true negative cases $P(N_{Camera} \& N_{CoCiP})$, where no contrails are observed (N_{Camera}) and predicted (N_{CoCiP}); (iii) false positive cases $P(N_{Camera} \& Y_{CoCiP})$, where contrails are predicted in the simulation but not observed; and (iv) false negative cases $P(Y_{Camera} \& N_{CoCiP})$, where contrails are observed but not predicted in the simulation. In instances where multiple observed contrail segments (Y_{Camera}) overlap and/or

are closely clustered together, we assign them to the respective ADS-B waypoints through manual visual inspection of preceding frames (Segrin et al., 2007). All ADS-B waypoints with Y_{Camera} are further classified based on their observed lifetimes, i.e., duration during which the contrail is present within the camera's field of view. The lifetime categories include: (i) short-lived contrails with observed lifetimes of fewer than 2 minutes; (ii) contrails with observed lifetimes of between 2 and 10 minutes; and (iii) persistent contrails with observed lifetimes of least 10 minutes (World Meteorological Organization, 2017).
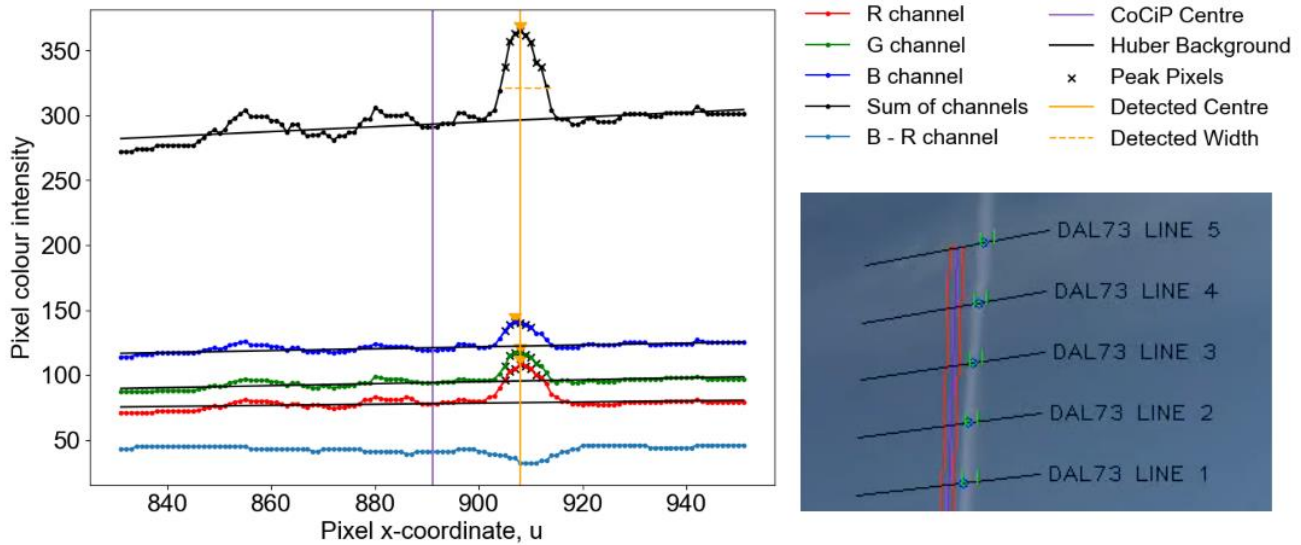
Figure 3: Pixel colour intensity profiles of the contrail waypoint at Line 5 (shown at the bottom right). Linear trendlines (in black) indicate the background colour intensity for each RGB channel. The solid vertical yellow and purple lines represent the mid-point of the observed and simulated contrail plume, respectively, while the dashed (horizontal) yellow line indicates the estimated contrail pixel width.

Additionally, for waypoints with true positive cases (Y_{Camera} & Y_{CoCiP}), we also compare their observed lifetimes and evolving contrail width relative to the simulated CoCiP outputs. To estimate the observed contrail pixel width from the video footage, we apply the Bresenham (2010) line drawing algorithm at each ADS-B waypoint to extract: (i) a line of pixels orthogonal to the flight trajectory; and (ii) the Red-Green-Blue (RGB) colour channel intensity of these pixels (Fig. 3). Previous studies found that the presence of clouds can be identified by their prominent increase in pixel intensity, especially in the red channel relative to the blue channel, because the sky scatters more blue than red light while clouds scatter both red and blue light equally (Long et al., 2006; Shields et al., 2013). However, due to day-to-day variability in atmospheric conditions, we were unable to consistently identify contrails from the video footage by applying a fixed threshold for the red-blue pixel intensity ratio. Instead, we compare the relative difference between the local pixel intensity ($P_{u,v}$) and the modelled background pixel intensity ($\hat{P}_{u,v}^{B}$),

$$\Delta P_{u,v} = P_{u,v} - \hat{P}_{u,v}^{B}, \tag{3}$$

where $\hat{P}_{u,v}^{B}$ is modelled using a Huber regression instead of a traditional least squares regression to minimise the regression sensitivity to outliers (Pedregosa et al., 2012). The observed contrail pixel width at each waypoint and time slice is then estimated from the video footage as follows,

$$\Delta P_{u,v} > \overline{\Delta P_{u,v}} + 2\sigma(\Delta P_{u,v}), \qquad (4)$$

175 where $\overline{\Delta P_{u,v}}$ and $\sigma(\Delta P_{u,v})$ are the mean and standard deviations of the line of pixels orthogonal to the flight trajectory respectively, and the mid-point of the observed plume determined by locating the local maximum of $\Delta P_{u,v}$ (Fig. 3). The reverse camera transformation is then applied to convert the 2D plane pixel width to a geometric width within a 3D space. Notably, due to the lack of depth information from a single camera, we assume that observed contrail altitude is equal to the modelled contrail altitude from CoCiP. This assumption introduces an additional source of error in the observed geometric contrail width

180 when compared to the pixel contrail width, which we discuss below.

3 Results and discussion

This section evaluates the simulated contrail formation (Section 3.1), lifetime (Section 3.2), and width (Section 3.3) from CoCiP relative to observations from the video footage. Where possible, we also incorporate additional variables into the analysis, such as the specific aircraft characteristics and local meteorology at each waypoint, to better understand the factors

185 influencing the agreement between the observed and simulated contrail properties.

3.1 Contrail formation

A total of 1,619 unique waypoints from 283 flights were identified across five days of video footage. Table 1 shows that the simulation correctly predicts the formation and absence of contrails for 69.3% of the flight waypoints, i.e., $P(Y_{Camera}$ & $Y_{CoCiP})$ of 32.9% + $P(N_{Camera}$ & $N_{CoCiP})$ of 36.4%. However, the percentage of false negative outcomes, $P(Y_{Camera}$ & $N_{CoCiP})$ = 25.9%,

190 is 5.4 times larger than the false positive outcome, $P(N_{Camera}$ & $Y_{CoCiP})$ = 4.8%, which suggests that the simulation exhibits a: (i) specificity of 88.3%, i.e., $P(N_{CoCiP}|N_{Camera}) = \frac{P(N_{Camera} \& N_{CoCiP})}{P(N_{Camera} \& N_{CoCiP}) + P(N_{Camera} \& Y_{CoCiP})}$ which is the proportion of actual negatives that is correctly predicted by the model; (ii) precision of 87.3%, i.e., $P(Y_{Camera}|Y_{CoCiP}) = \frac{P(Y_{Camera} \& Y_{CoCiP})}{P(Y_{Camera} \& Y_{CoCiP}) + P(N_{Camera} \& Y_{CoCiP})}$ which is the proportion of predicted positives that are true positives; and (iii) sensitivity of 56.0%, i.e., $P(Y_{CoCiP}|Y_{Camera}) = \frac{P(Y_{Camera} \& Y_{CoCiP})}{P(Y_{Camera} \& Y_{CoCiP}) + P(Y_{Camera} \& N_{CoCiP})}$ which is the proportion of actual positives that are

195 correctly predicted by the model. In other words, the simulation is more likely to correctly predict the observed outcomes on the presence/absence of contrails (high specificity and precision), but it could underestimate the observed contrail formation (low sensitivity).

We evaluate the impact of aircraft cruise altitude on contrail observations and model performance (Fig. 4a). In general, contrails are most likely to be observed by the camera at altitudes between 34,000 and 38,000 ft where $P(Y_{Camera}) > 60\%$. Across all

200   altitudes, the false positive rate, $P(Y_{CoCiP}|N_{Camera}) = \frac{P(Y_{CoCiP} \& N_{Camera})}{P(Y_{CoCiP} \& N_{Camera}) + P(N_{CoCiP} \& N_{Camera})}$, tends to range between 0% and 25%.

Two factors likely contribute to this error: (i) the known limitations in the ERA5 HRES humidity fields (Teoh et al., 2022a; Agarwal et al., 2022; Reutter et al., 2020); and (ii) sub-grid scale RHi variabilities that cannot currently be resolved from the spatiotemporal resolution of the ERA5 HRES (0.25° longitude × 0.25° latitude over 37 pressure levels provided at hourly time intervals) (Irvine et al., 2014; Teoh et al., 2022a). For (i), although corrections were applied to the humidity fields to ensure

205   that the RHi distribution from the ERA5 HRES is consistent with in-situ measurements (Section 2.2.2), we note that the RHi uncertainties and errors remains large at the waypoint level (Teoh et al., 2023).

Table 1: Summary statistics for each day when contrails were observed by the camera, and a comparison of the contrail formation predictive accuracy from CoCiP relative to the camera observations for each day. The notation Y_{Camera} indicates that the camera observed contrails forming at the flight waypoint, N_{Camera} indicates that no contrails at the flight waypoint were observed by the
210   **camera, Y_{CoCiP} indicates that the CoCiP simulation estimates the formation of contrails at the flight waypoint, while N_{CoCiP} indicates that the CoCiP simulation did not predict contrails forming at the flight waypoint.**

Date	Hours	Number of flights	Number of waypoints	Waypoints				
				$P(Y_{Camera}$ & $Y_{CoCiP})$	$P(N_{Camera}$ & $Y_{CoCiP})$	$P(Y_{Camera}$ & $N_{CoCiP})$	$P(N_{Camera}$ & $N_{CoCiP})$	Correct prediction*
05-Nov-2021	2	62	328	25.3%	7.3%	13.4%	54.0%	79.3%
09-Nov-2021	2	39	227	43.2%	7.9%	18.9%	30.0%	73.2%
14-Jan-2022	4	39	215	0.0%	0.0%	58.1%	41.9%	41.9%
26-Feb-2022	3	73	420	38.6%	0.2%	26.0%	35.2%	73.8%
10-Apr-2022	3	70	429	44.3%	7.9%	23.1%	24.7%	69.0%
TOTAL	**14**	**283**	**1619**	**32.9%**	**4.8%**	**25.9%**	**36.4%**	**69.3%**

* The correct prediction is calculated by $P(Y_{Camera}$ & $Y_{CoCiP}) + P(N_{Camera}$ & $N_{CoCiP})$.

The false negative rate, $P(N_{CoCiP}|Y_{Camera}) = \frac{P(N_{CoCiP} \& Y_{Camera})}{P(N_{CoCiP} \& Y_{Camera}) + P(Y_{CoCiP} \& Y_{Camera})}$, exhibits a negative linear relationship with altitude, where $P(N_{CoCiP}|Y_{Camera})$ is: (i) above 80% at altitudes below 30,000 feet, meaning that a significant fraction of contrails

215   observed at lower altitudes are not being predicted in the simulation; (ii) around 50–80% between 30,000 and 38,000 feet; and (iii) below 30% at altitudes above 38,000 feet (Fig. 4a). These error patterns can most likely be attributed to the warmer temperatures at lower altitudes resulting in $T_{amb} \approx T_{SAC}$ (Reutter et al., 2020), where: (i) small errors in T_{amb} and the estimated T_{SAC} is likely to have a significant impact on contrail formation predictions; and (ii) the microphysics of soot activation at $T_{amb} \approx T_{SAC}$ becomes strongly dependent on various soot properties such as the geometric-mean dry core radius and hygroscopicity

220   (Bier et al., 2022), but CoCiP does not currently account for these effects. Indeed, a comparison between the difference in ambient and SAC threshold temperature ($dT_{SAC} = T_{amb} - T_{SAC}$) shows that the false discovery rate, $P(N_{Camera}|Y_{CoCiP}) = \frac{P(N_{Camera} \& Y_{CoCiP})}{P(N_{Camera} \& Y_{CoCiP}) + P(Y_{Camera} \& Y_{CoCiP})}$, is largest when $dT_{SAC} > $ -2.5 K (77.2%), and smallest when $dT_{SAC} < $ -10 K (9.3%) (Fig. 4b).
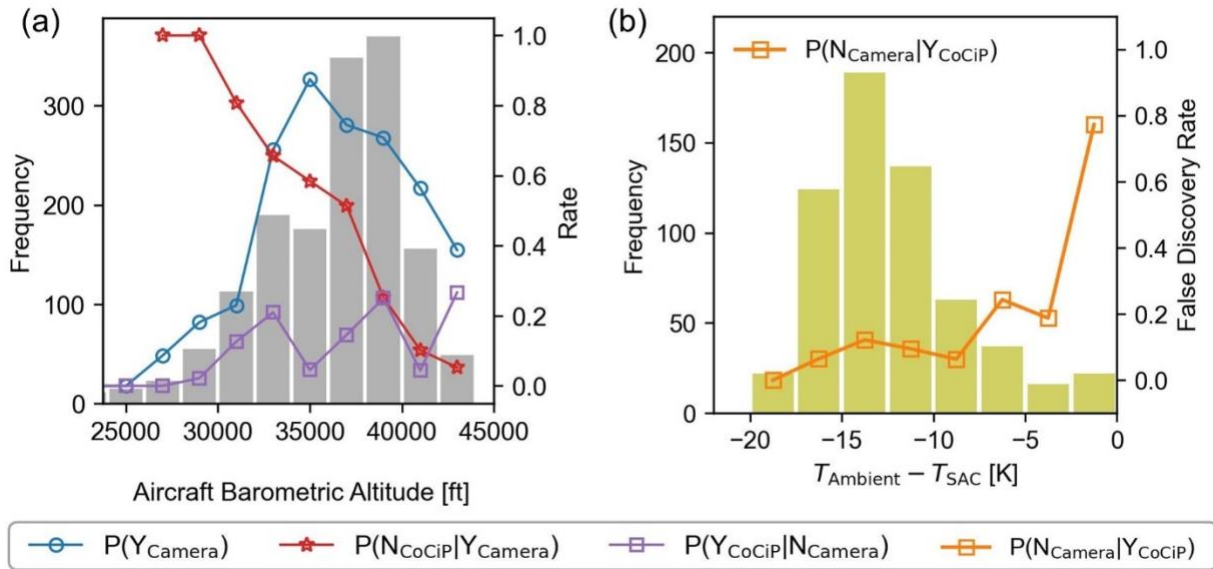
225

Figure 4: Probability density function of the: (a) aircraft barometric altitude; and (b) difference between the ambient and SAC threshold temperature for ADS-B waypoints with observed and/or simulated contrails. Additional statistics on probability of waypoints with contrail observations, $P(Y_{Camera})$ (blue line), and conditional probabilities $P(N_{CoCiP}|Y_{Camera})$ (red line), $P(Y_{CoCiP}|N_{Camera})$ (purple line), and $P(N_{Camera}|Y_{CoCiP})$ (orange line) are also included in these figures.

230   **3.2 Contrail observed lifetime**

Among the 953 unique waypoints with observed contrails (Y_{Camera}), 72.8% of the contrails formed are short-lived (< 2 min), 10.6% of them are contrails with observed lifetimes of between 2 and 10 minutes, and 16.6% of them are persistent contrails with observed lifetimes exceeding 10 minutes. A further evaluation of these waypoints (Y_{Camera}) shows a weak negative correlation between dT_{SAC} and the observed contrail lifetime (R=-0.168, as shown in Fig. 5). This finding is consistent with

235   previous research, suggesting that contrails forming at lower temperatures tend to have a lower ice water content and smaller ice crystal radius which, in turn, can increase the contrail lifetime (Teoh et al., 2022a).

Fig. 6 shows that the false negative rate, $P(N_{CoCiP}|Y_{Camera})$, tends to decrease with increasing aircraft cruise altitude and the observed contrail lifetime. $P(N_{CoCiP}|Y_{Camera})$ is: (i) lowest for persistent contrails (observed lifetime > 10 min) forming above 35,000 feet, where $P(N_{CoCiP}|Y_{Camera}) < 5\%$; and (ii) largest for short-lived contrails (observed lifetimes < 2 min) forming below

240   35,000 feet, where $P(N_{CoCiP}|Y_{Camera}) > 75\%$. Consequently, around 92% of all waypoints with a false negative outcome, $P(N_{CoCiP}$ & $Y_{Camera})$, are associated with short-lived contrails (< 2 min). The contrail simulation also exhibits a low sensitivity, $P(Y_{CoCiP}|Y_{Camera}) = 44.5\%$, when the observed contrails are short-lived (< 2 min), but the sensitivity increases by approximately twofold to 86.5% when contrails have an observed lifetimes of > 2 min.
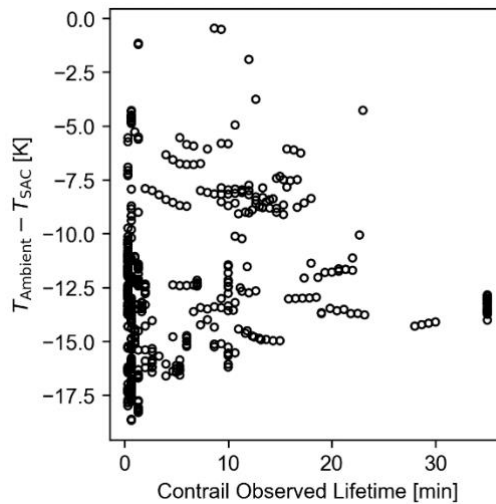
Figure 5: Comparison of the observed contrail lifetime versus the difference between the ambient temperature (T_{amb}) and SAC threshold temperature (T_{SAC}) for individual ADS-B flight waypoints with true positive cases (Y_{Camera} & Y_{CoCiP}).
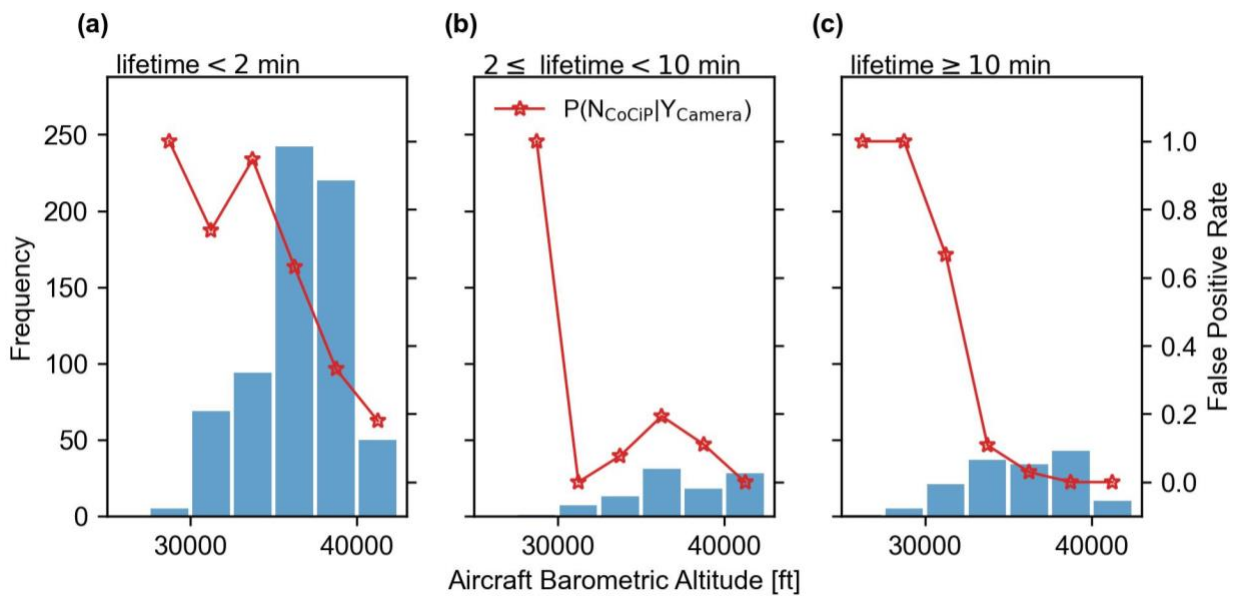
Figure 6: Histogram of the aircraft altitudes for ADS-B waypoints with observed contrails and their respective false positive rates (red lines) at each altitude bins. The waypoints are segmented into three groups based on their observed contrail lifetime: (a) short-lived contrails (< 2 mins); (b) contrails that persist for 2–10 mins; and (c) persistent contrails (≥ 10 mins).

3.3 Contrail width

Fig. 2 illustrates the temporal evolution of the observed and simulated contrails that were formed by one flight, while Fig. 7 compares the observed contrail pixel and geometric width relative to the simulated CoCiP outputs for 533 segments from all waypoints with true positive cases (Y_{Camera} & Y_{CoCiP}). Our findings, as assessed by the root mean square error (RMSE) metric,

255   suggest that the simulated contrail width tends to be smaller than the observed pixel width (by -6.8 pixels) and geometric width (by -330 m). These results are consistent with Schumann et al. (2013) and could be caused by the: (i) potential underestimation of sub-grid scale wind shear and turbulent mixing in the ERA5 HRES; and (ii) CoCiP's assumption of a Gaussian plume when simulating the evolution of contrails (Schumann, 2012).

A visual comparison shows that the agreement between the observed and simulated contrail geometric width (Fig. 7b) is lower
260   than the pixel width (Fig. 7a). The higher relative agreement between the observed and simulated contrail pixel width is partially explained by its dependence on the contrail-camera distance, i.e., contrails further away have a smaller pixel width, which can be estimated with high accuracy. In contrast, our estimate of the observed geometric width assumes that the: (i) actual contrail altitude is equal to the simulated contrail altitude in CoCiP (Section 2.4); and (ii) contrail cross-section is a horizontal ellipse, meaning that the contrail edges are at the same altitude as the contrail mid-point. Assumption (i) is subject
265   to uncertainties in the actual aircraft mass, resulting in additional errors when simulating the contrail vertical displacement caused by the wake vortex downwash; while assumption (ii) does not hold in the real world due to local turbulence and wind shear that can deform the contrail cross-section into an inclined ellipse. To evaluate their impacts, we assess the sensitivity of the observed contrail geometric width by varying the assumed contrail altitude by ± 100 m for assumption (i), and by ± 100 m at one of the contrail edges for assumption (ii). Our results indicate that assumption (ii) has a significantly greater influence
270   on the observed contrail geometric width (± 36%) relative to assumption (i) (± 0.9%).
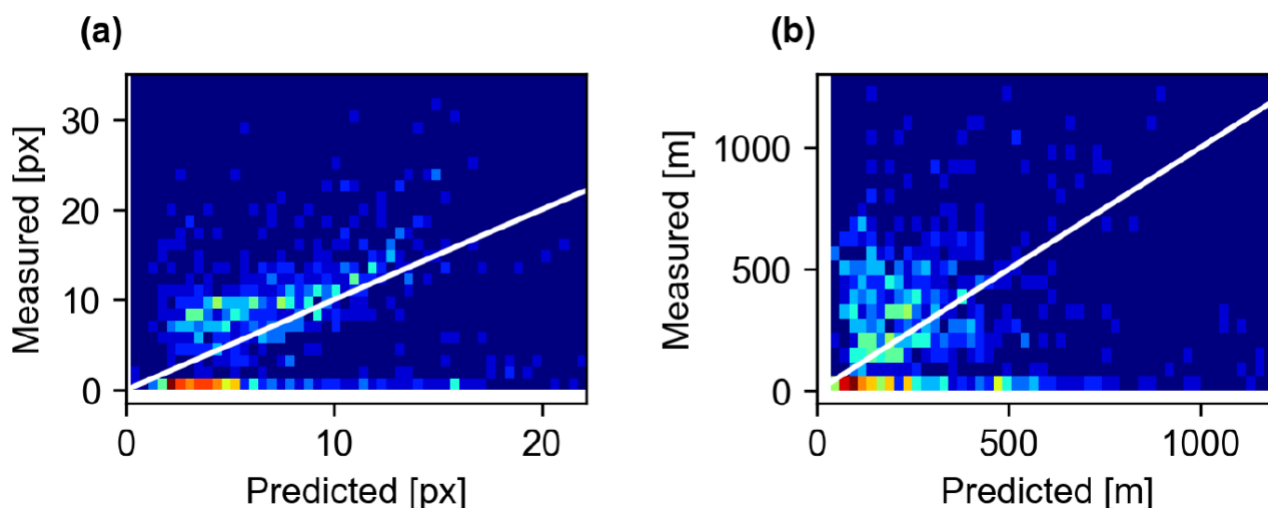
Figure 7: Kernal density estimate between the observed and simulated contrail: (a) pixel width; and (b) geometric width for ADS-B waypoints with true positive cases (Y_{Camera} & Y_{CoCiP}).

We also examined contrails that were initially formed outside the spatial domain and were subsequently advected into the
275   camera's field of view, where the results yielded mixed outcomes. For instance, upon visual inspection, contrails predicted on the 5th of November 2021 at 09:09:20 UTC appear to show a reasonable agreement relative to observations (Fig. 8b). In contrast, on the 9th of November 2021 at 10:02:40 UTC, the simulation predicted the presence of contrail cirrus with a mean

optical depth of 0.024 [0.002, 0.056] (5th and 95th percentile), suggesting that these contrails are below and close to the lower visibility limit threshold for ground-based observers (optical depth of < 0.02) (Kärcher et al., 2009). While faint white grains

280 were visible in the video footage (Fig. 8a), discerning whether these features represented contrail cirrus, natural clouds, or false positive cases (N_{Camera} & Y_{CoCiP}) is challenging. Collectively, our results suggest that ground-based cameras generally excel at identifying freshly formed and narrow contrails relative to satellites, but they are likely to also encounter difficulties in detecting optically thin contrails below a threshold optical depth that is yet to be determined.

4 Discussion and conclusions

285 Recent estimates suggest that the 2019 global annual mean contrail cirrus net RF (62.1 [34.8, 74.8] mW m^{-2}) (Teoh et al., 2023) could be two times larger than the RF from aviation's cumulative CO_2 emissions (34.3 [31, 38] mW m^{-2}) (Lee et al., 2021). Ground-based cameras provide a cost-effective way to observe contrails, and unlike satellite imagery, their higher relative spatiotemporal resolution enables effective tracking of the formation and evolution of young contrails. Moreover, these ground-based observations can also be used to validate specific aspects of existing contrail models, which currently play a

290 crucial role in validating and evaluating the effectiveness of different climate mitigation strategies.

In this study, we develop a methodology to track and analyse contrails from ground-based video footage, and subsequently compare these observations with contrail simulations. The ground-based contrail observations consist of 14 h of video footage recorded on five different days at Imperial College London's South Kensington Campus, and the actual flight trajectories that intersect with the camera's field of view were obtained from ADS-B telemetry. In total, 1,619 ADS-B waypoints from 283

295 flights were identified from the video footage, and contrails that were formed from these flights were simulated with CoCiP using historical meteorology from the ECMWF ERA5 HRES reanalysis; and estimates of the aircraft fuel consumption and aircraft-engine specific nvPM particle number emissions from ADS-B transponder data.

The simulation accurately forecasted the formation (Y_{Camera} & Y_{CoCiP}) and absence (N_{Camera} & N_{CoCiP}) of contrails in 69.3% of the ADS-B waypoints (Table 1), and the best agreement between the observations and simulations occur when contrails: (i)

300 have an observed lifetime of > 2 min; (ii) were formed between 35,000 and 40,000 feet; and (iii) at temperatures where dT_{SAC} < -10 K (Fig. 4 and 6). However, a comparison between the waypoints with false negative and false positive outcomes, i.e., P(Y_{Camera} & N_{CoCiP}) = 25.9% vs. P(N_{Camera} & Y_{CoCiP}) = 4.8%, suggests that the simulation underestimates contrail occurrence. Instances where a contrail is observed but not predicted occur five times more often than instances where the model falsely predicts a contrail to form (25.9/4.8 = 5.4). Around 92% of waypoints with false negative outcomes, P(N_{CoCiP} & Y_{Camera}), are

305 associated with short-lived contrails (< 2 min) that were formed at altitudes below 30,000 feet and at temperatures where dT_{SAC} > -2.5 K (Fig. 4 and 6). Among waypoints with true positive cases, P(Y_{Camera} & Y_{CoCiP}), we also evaluated the evolving contrail dimensions over time and found that the simulation underestimates the geometric contrail width by an average of 17.5%. This underestimation is most3 likely caused by two factors: (i) the sub-grid scale variability in wind shear and turbulent mixing that

cannot be resolved from the spatiotemporal resolution of numerical weather prediction (NWP) models; and (ii) CoCiP's
310 assumption of a horizontal ellipse as the shape of the contrail cross-section, which may not adequately represent the inclined
ellipse observed in real-world conditions.
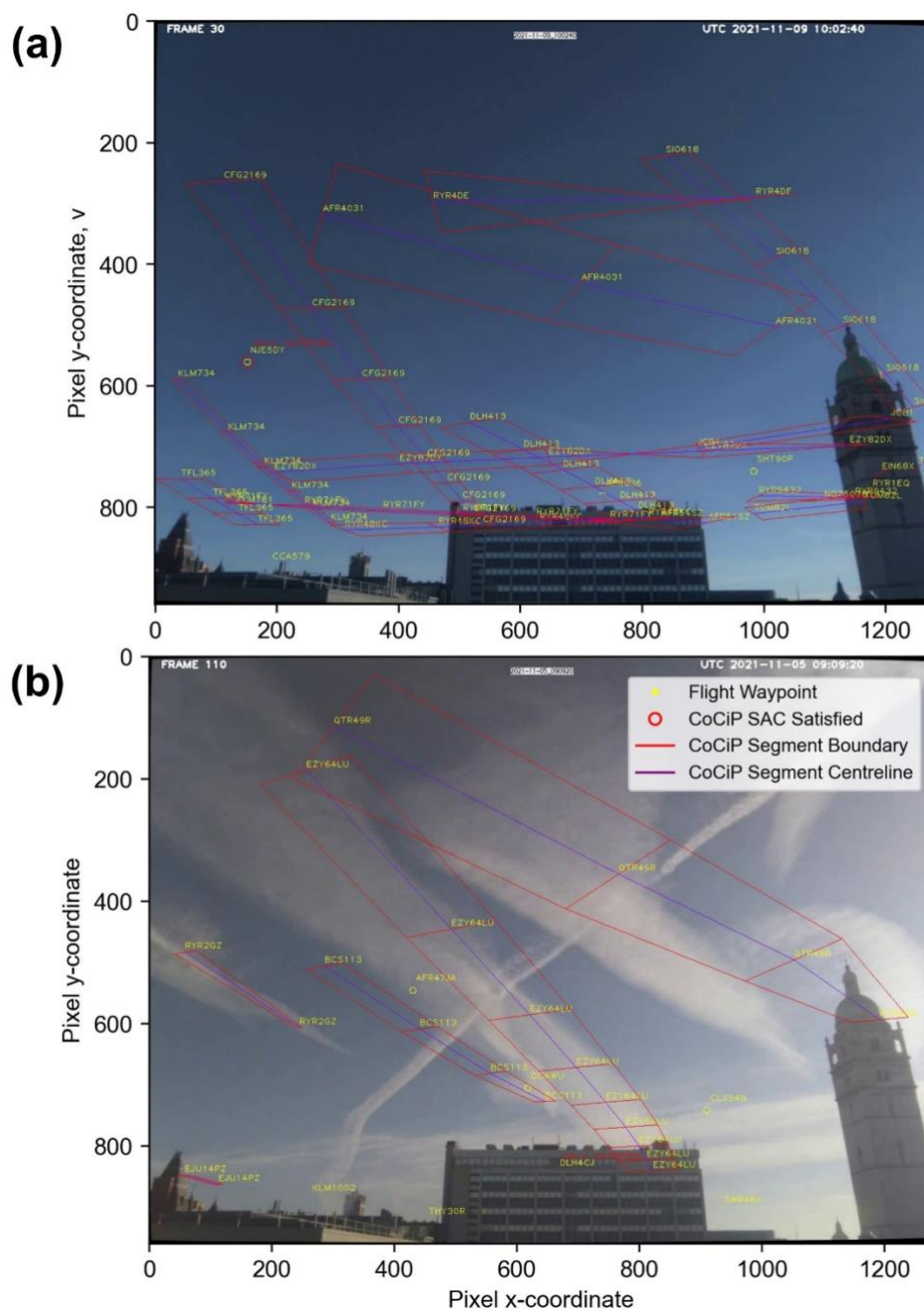
Figure 8: Examples of contrails that were initially formed outside the spatial domain and subsequently advected into the camera's field of view on the: (a) 5-Nov-2021 at 09:09:20 UTC; and (b) 9- Nov-2021 at 10:02:40 UTC.

315   When taken together, these results hold potential significance within the context of contrail mitigation because: (i) contrails I forming at very low temperatures (dT_{SAC} < -10 K) tend to be long-lived and strongly warming (Teoh et al., 2022a) and are more likely to be captured by the contrail simulation; while (ii) contrails forming at warmer temperatures (dT_{SAC} > -2.5 K), where the simulation exhibits a larger relative error, are generally short-lived (< 2 min) with a negligible energy forcing (Teoh et al., 2020a). Nevertheless, we also acknowledge the potential limitations of our study, such as the: (i) small sample size; and

320   (ii) inherent bias in selecting contrails formed in high-pressure systems (i.e., clear sky conditions), while excluding contrails formed in low-pressure systems associated with storms and/or overcast weather. For limitation (ii), the distinct synoptic weather conditions could lead to different error patterns in the NWP which will propagate to the simulated contrail outputs. Future work can build upon our research by: (i) establishing a network of ground-based cameras to observe contrails across a larger set of flights and over a wider domain and to reduce camera model sensitivity to contrail altitude; (ii) conducting a larger

325   scale comparison between the observed and simulated contrail formation to assess the accuracy of humidity fields provided by NWP models, which is a critical input parameter for contrail models; (iii) combining ground-based and satellite observations to track the whole contrail lifecycle, which can then be used to validate existing contrail models; and (iv) integrating ground-based observations with contrail forecasts, thereby reducing the uncertainties in the real-time decision making processes for flight diversions to minimise the formation of strongly warming contrails.

330   **Appendix**

A1 Video footage classification

Temporal variabilities in weather conditions influence the suitability of the video footage for contrail observations. To filter the video footage that can be used to observe, track, and extract the properties of contrails, we visually inspect each hourly recordings and classify them based on the background cloud cover (Table A1) and lighting conditions (Table A2). An example of each classification

335   is shown in Fig. A1. The 14 h of video footage that were selected for further analysis have: (i) clear sky conditions; and (ii) optimal lighting with strong color contrast between the (blue) sky and (white) contrails. Following the selection of video footages that are feasible for contrail analysis, we reduced their frame rate to 40 seconds per frame to match the temporal resolution of the ADS-B data and CoCiP outputs. The camera transformation model, as will be described in Appendix A3, was applied to systematically superimpose ADS-B data and CoCiP outputs onto the video footage.

340   **Table A1: Classification of the video footage by the extent of background cloud cover.**

Category	Remarks/Implications
Clear	• Clear sky conditions (0 oktas)* with an absence of low-, mid- and high-level cirrus.
Presence of low- and mid-level clouds	• Cloud cover with more than 5 oktas* can potentially obscure contrail observations, thereby limiting the opportunities for analysis.
Presence of high-level clouds	• Contrails formed within these clouds may be difficult to identify. • Contrails formed outside and subsequently advected into the camera's field of view may not be easily distinguished from natural cirrus clouds.

*: The unit "okta" is used to quantify the extent of cloud cover by dividing the sky into eights. A measurement of 0 oktas denotes a completely clear sky, while 8 oktas imply an entirely overcast sky.
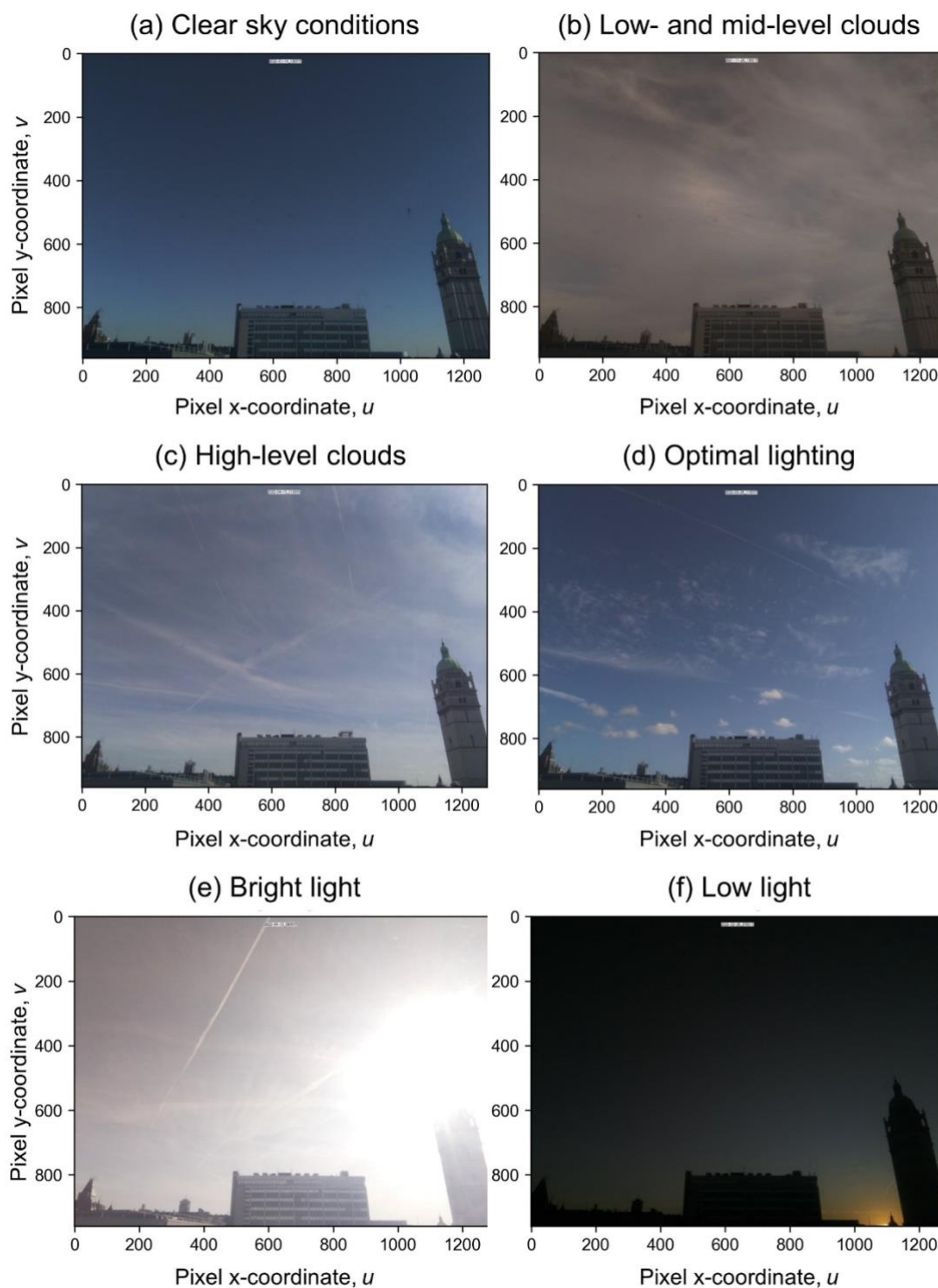
Figure A1: Examples of the different background cloud cover, i.e., (a) clear sky conditions, (b) low-/mid-level clouds, and (c) high-level clouds), and lighting conditions, i.e., (d) optimal lighting, (e) bright-light; and (f) low-light conditions that were described in Tables A1 and A2.

Table A2: Classification of the video footage by the ambient lighting levels.

Category	Remarks/Implications
Optimal	• Strong color and feature contrast between the (blue) sky and contrails, ideal for contrail observations.
Bright light	• Limited color contrast between the (white) sky compared to contrails and natural cirrus clouds. • If the sun is in direct view of the camera, the solar glare may obscure a portion of the image.
Low light	• Adjustments to the typical thresholds used to identify contrails will be necessary due to the reduced color brightness of the contrail against a darker background.

A2 Corrections to camera distortion

350 Unlike the ideal pinhole model, camera images contain radial and tangential distortion. Radial distortion occurs due to the bending of light rays near the edge of a lens, causing straight lines to appear curved. Tangential distortion occurs when lens assembly are not directly parallel and centred over the image plane. Distortion coefficients are determined using a chessboard pattern and homography, and an example process can be found in Wu et al. (2015). Using the OpenCV Python package (Bradski, 2000), every pixel is mapped to a corrected position following these steps:

355 **STEP 1**: The distorted pixel coordinates (u_dist, v_dist) are converted to distorted camera coordinates (x_dist, y_dist, z_dist) in Eq. (A1) using the inverse of the camera intrinsic matrix (K^{-1}, see Appendix A3),

$$\begin{bmatrix} x_\text{dist} \\ y_\text{dist} \\ z_\text{dist} \end{bmatrix} = K^{-1} \begin{bmatrix} u_\text{dist} \\ v_\text{dist} \\ 1 \end{bmatrix}. \tag{A1}$$

STEP 2: The distorted camera coordinates are corrected using Eq. (A2) and Eq. (A3), both of which are found in the OpenCV package documentation,

360
$$x'' = x'(1 + k_1 r^2 + k_2 r^4 + k_3 r^6) + [2p_1 x'y' + p_2(r^2 + 2x'^2)], \tag{A2}$$

$$y'' = y'(1 + k_1 r^2 + k_2 r^4 + k_3 r^6) + [2p_2 x'y' + p_1(r^2 + 2x'^2)], \tag{A3}$$

where $x' = x_\text{dist}/z_\text{dist}$ and $y' = y_\text{dist}/z_\text{dist}$ are normalised coordinates, $r = \sqrt{x'^2 + y'^2}$, $k_1 = 0.580$, $k_2 = -2.661$, and $k_3 = 4.420$ are radial distortion coefficients, and $p_1 = 5.803 \times 10^{-1}$ and $p_2 = -2.576 \times 10^{-3}$ are tangential distortion coefficients.

365 **STEP 3**: The undistorted pixel coordinates (u, v) are recalculated using Eq. (A4),

$$\lambda \begin{bmatrix} u \\ v \\ z_\text{dist} \end{bmatrix} = K \begin{bmatrix} x'' \\ y'' \\ z'' \end{bmatrix}. \tag{A4}$$

Fig. A2 shows an original frame captured by the camera alongside a corrected frame using the three-step process. While these differences may not be visually discernible, it is crucial to remove distortions to minimise errors when extracting the observed contrail pixel and geometric width from these images. The correction of the minor distortion in the original frame is evident

370 through the added grid lines. All video footage used in the study underwent initial frame-by-frame processing to eliminate

distortion before conducting subsequent analysis.
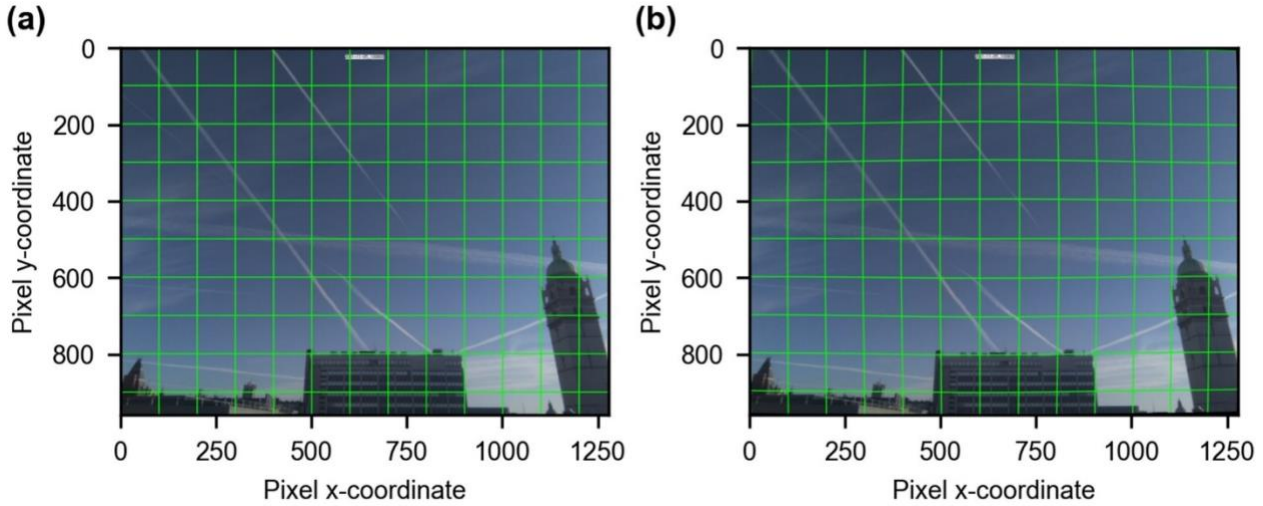
Figure A2: Side-by-side comparison of (a) an original frame captured by the ground-based camera; and (b) the distortion corrected frame by mapping coordinates to their undistorted positions using the OpenCV Python package.

375 **A3 Camera transformation model**

After correcting for distortions, a camera transformation method is used to project the aircraft positions and simulated contrail

location, which are provided as three-dimensional (3D) positions, to the camera observations which utilises a two-dimensional

(2D) pixel coordinate (u, v). A two-step process is used to achieve this:

STEP 1: The real-world 3D positions relative to the camera is mapped to a 3D camera coordinate system (X, Y, Z) using an

380 extrinsic (rotation) matrix R,

$$R = [R_x][R_y][R_z] = \begin{bmatrix} 0.1434 & -0.1357 & 0.9803 \\ -0.1357 & 0.9785 & 0.1553 \\ -0.9803 & -0.1553 & 0.1219 \end{bmatrix}. \tag{A5}$$

R describes the camera rotation in relation to the world axis, where R_x, R_y, and R_z are the roll, pitch, and yaw of the camera

respectively. The R coefficients are estimated by minimising the residuals between the computed and measured pixel

coordinates of known aircraft positions and landmarks that are visible in the camera frame.

385 **STEP 2**: The 3D camera coordinates is then transformed to a 2D pixel coordinate system (u, v) using an intrinsic (camera)

matrix K,

$$K = \begin{bmatrix} f_x & s & x_0 \\ 0 & f_y & y_0 \\ 0 & 0 & 1 \end{bmatrix} = \begin{bmatrix} 708 & 0 & 634 \\ 0 & 708 & 472 \\ 0 & 0 & 1 \end{bmatrix}, \tag{A6}$$

where the camera parameters f_x and f_y are the focal lengths in pixel units, (x_0, y_0) is the principal point of the image, and s represents the axis skew. Fig. 2 in the main text provides an example of the superimposed flight trajectories and simulated contrail properties to the video footage.

Author contributions

MEJS and EG conceptualised the study. JL, RT, and EG developed the methodology and undertook the investigation. JL, RT, JP, EG, and MS were responsible for software development and data curation. JL and RT created or sourced the figures. JL and RT wrote the original manuscript. MEJS, EG, and MS acquired funding. All authors have read, edited, and reviewed the manuscript, and agreed upon the published version of the paper.

Funding acknowledgements

EG was supported by a Royal Society University Research Fellowship (URF/R1/191602) and NERC project RECFI-4D (NE/X012255/1).

Data availability

The ADS-B telemetry that is used to derive the actual flight trajectories in this study was purchased from Spire Aviation and can be made available for scientific research upon reasonable request. The pycontrails repository that contains the CoCiP algorithm has recently been published and publicly available at https://doi.org/10.5281/zenodo.7776686. This document used elements of Base of Aircraft Data (BADA) Family 4 Release 4.2 which has been made available by EUROCONTROL to Imperial College London. EUROCONTROL has all relevant rights to BADA. ©2019 The European Organisation for the Safety of Air Navigation (EUROCONTROL). EUROCONTROL shall not be liable for any direct, indirect, incidental, or consequential damages arising out of or in connection with this document, including the use of BADA. This document contains Copernicus Climate Change Service information 2023. Neither the European Commission nor ECMWF is responsible for any use of the Copernicus information. The timelapse videos will be submitted to the Central for Environmental Data Analysis (CEDA) on acceptance.

Competing interests

There are no conflicts of interest and all funding sources have been acknowledged. All figures are our own. None of the authors has any competing interests.

References

Agarwal, A., Meijer, V. R., Eastham, S. D., Speth, R. L., and Barrett, S. R. H.: Reanalysis-driven simulations may overestimate persistent contrail formation by 100-250%, Environmental Research Letters, 17, 1–14, https://doi.org/10.1088/1748-9326/AC38D9, 2022.

Bier, A. and Burkhardt, U.: Impact of Parametrizing Microphysical Processes in the Jet and Vortex Phase on Contrail Cirrus Properties and Radiative Forcing, Journal of Geophysical Research: Atmospheres, 127, e2022JD036677, https://doi.org/10.1029/2022JD036677, 2022.

Bier, A., Unterstrasser, S., and Vancassel, X.: Box model trajectory studies of contrail formation using a particle-based cloud microphysics scheme, Atmos Chem Phys, 22, 823–845, https://doi.org/10.5194/ACP-22-823-2022, 2022.

Bock, L. and Burkhardt, U.: Reassessing properties and radiative forcing of contrail cirrus using a climate model, Journal of Geophysical Research: Atmospheres, 121, 9717–9736, https://doi.org/10.1002/2016JD025112, 2016.

Boulanger, D., Bundke, U., Gallagher, M., Gerbig, C., Hermann, M., Nédélec, P., Rohs, S., Sauvage, B., Ziereis, H., Thouret, V., and Petzold, A.: IAGOS Time series [Data set], AERIS, https://doi.org/https://doi.org/10.25326/06, 2022.

Bradski, G.: The OpenCV Library: Dr. Dobb's Journal of Software Tools, https://www.bibsonomy.org/bibtex/25fa6cccd386170d95ae17fd29a42303d/ross_mck (last access: 18 August 2023), 2000.

Bresenham, J. E.: Algorithm for computer control of a digital plotter, IBM Systems Journal, 4, 25–30, https://doi.org/10.1147/SJ.41.0025, 2010.

Burkhardt, U., Bock, L., and Bier, A.: Mitigating the contrail cirrus climate impact by reducing aircraft soot number emissions, NPJ Clim Atmos Sci, 1, 1–7, https://doi.org/10.1038/s41612-018-0046-4, 2018.

Caiazzo, F., Agarwal, A., Speth, R. L., and Barrett, S. R. H.: Impact of biofuels on contrail warming, Environmental Research Letters, 12, 114013, https://doi.org/https://doi.org/10.1088/1748-9326/aa893b, 2017.

Chen, C. C. and Gettelman, A.: Simulated radiative forcing from contrails and contrail cirrus, Atmos Chem Phys, 13, 12525–12536, https://doi.org/10.5194/acp-13-12525-2013, 2013.

Dietmüller, S., Matthes, S., Dahlmann, K., Yamashita, H., Simorgh, A., Soler, M., Linke, F., Lührs, B., Meuser, M. M., Weder, C., Grewe, V., Yin, F., and Castino, F.: A Python library for computing individual and merged non-CO_2 algorithmic climate change functions: CLIMaCCF V1.0, Geosci Model Dev, 16, 4405–4425, https://doi.org/10.5194/GMD-16-4405-2023, 2023.

Duda, D. P., Bedka, S. T., Minnis, P., Spangenberg, D., Khlopenkov, K., Chee, T., and Smith, W. L.: Northern Hemisphere contrail properties derived from Terra and Aqua MODIS data for 2006 and 2012, Atmos Chem Phys, 19, 5313–5330, https://doi.org/10.5194/ACP-19-5313-2019, 2019.

EASA: ICAO Aircraft Engine Emissions Databank (07/2021), EASA [data set]: https://www.easa.europa.eu/domains/environment/icao-aircraft-engine-emissions-databank (last access: 17 August 2021), 2021.

445 ECMWF: The Copernicus Programme: Climate Data Store, ECMWF [data set], https://cds.climate.copernicus.eu/#!/home (last access: 15 February 2022), 2021.

EUROCONTROL: User Manual for the Base of Aircraft Data (BADA) Family 4. EEC Technical/Scientific Report No. 12/11/22-58. EUROCONTROL Experimental Centre (EEC), https://www.eurocontrol.int/model/bada (last access: 17 August 2021), 2016.

450 Feister, U., Möller, H., Sattler, T., Shields, J., Görsdorf, U., and Güldner, J.: Comparison of macroscopic cloud data from ground-based measurements using VIS/NIR and IR instruments at Lindenberg, Germany, Atmos Res, 96, 395–407, https://doi.org/10.1016/J.ATMOSRES.2010.01.012, 2010.

Fuglestvedt, J. S., Shine, K. P., Berntsen, T., Cook, J., Lee, D. S., Stenke, A., Skeie, R. B., Velders, G. J. M., and Waitz, I. A.: Transport impacts on atmosphere and climate: Metrics, Atmos Environ, 44, 4648–4677,
455 https://doi.org/10.1016/j.atmosenv.2009.04.044, 2010.

Grewe, V., Frömming, C., Matthes, S., Brinkop, S., Ponater, M., Dietmüller, S., Jöckel, P., Garny, H., Tsati, E., Dahlmann, K., Søvde, O. A., Fuglestvedt, J., Berntsen, T. K., Shine, K. P., Irvine, E. A., Champougny, T., and Hullah, P.: Aircraft routing with minimal climate impact: the REACT4C climate cost function modelling approach (V1.0), Geosci Model Dev, 7, 175–201, https://doi.org/10.5194/gmd-7-175-2014, 2014.

460 Grewe, V., Matthes, S., Frömming, C., Brinkop, S., Jöckel, P., Gierens, K., Champougny, T., Fuglestvedt, J., Haslerud, A., and Irvine, E.: Feasibility of climate-optimized air traffic routing for trans-Atlantic flights, Environmental Research Letters, 12, 34003, https://doi.org/10.1088/1748-9326/aa5ba0, 2017.

Gryspeerdt, E., Stettler, M. E. J., Teoh, R., Burkhardt, U., Delovski, T., and Painemal, D.: Operational choices produce larger contrail climate impacts from more fuel efficient aircraft [Submitted], Environmental Research Letters, 2023.

465 Haywood, J. M., Allan, R. P., Bornemann, J., Forster, P. M., Francis, P. N., Milton, S., Rädel, G., Rap, A., Shine, K. P., and Thorpe, R.: A case study of the radiative forcing of persistent contrails evolving into contrail-induced cirrus, Journal of Geophysical Research: Atmospheres, 114, https://doi.org/10.1029/2009JD012650, 2009.

Hersbach, H., Bell, B., Berrisford, P., Hirahara, S., Horányi, A., Muñoz-Sabater, J., Nicolas, J., Peubey, C., Radu, R., Schepers, D., Simmons, A., Soci, C., Abdalla, S., Abellan, X., Balsamo, G., Bechtold, P., Biavati, G., Bidlot, J., Bonavita, M., De Chiara,
470 G., Dahlgren, P., Dee, D., Diamantakis, M., Dragani, R., Flemming, J., Forbes, R., Fuentes, M., Geer, A., Haimberger, L., Healy, S., Hogan, R. J., Hólm, E., Janisková, M., Keeley, S., Laloyaux, P., Lopez, P., Lupu, C., Radnoti, G., de Rosnay, P., Rozum, I., Vamborg, F., Villaume, S., and Thépaut, J. N.: The ERA5 global reanalysis, Quarterly Journal of the Royal Meteorological Society, 146, 1999–2049, https://doi.org/10.1002/qj.3803, 2020.

Holzapfel, F.: Probabilistic Two-Phase Wake Vortex Decay and Transport Model, J Aircr, 40, 323–331,
475 https://doi.org/10.2514/2.3096, 2003.

Irvine, E. A., Hoskins, B. J., and Shine, K. P.: A Lagrangian analysis of ice-supersaturated air over the North Atlantic, Journal of Geophysical Research: Atmospheres, 119, 90–100, https://doi.org/10.1002/2013JD020251, 2014.

Jensen, E. J., Toon, O. B., Kinne, S., Sachse, G. W., Anderson, B. E., Chan, K. R., Twohy, C. H., Gandrud, B., Heymsfield, A., and Miake-Lye, R. C.: Environmental conditions required for contrail formation and persistence, Journal of Geophysical
480   Research: Atmospheres, 103, 3929–3936, https://doi.org/10.1029/97JD02808, 1998.

Jeßberger, P., Voigt, C., Schumann, U., Sölch, I., Schlager, H., Kaufmann, S., Petzold, A., Schäuble, D., and Gayet, J.-F.: Aircraft type influence on contrail properties, Atmos Chem Phys, 13, 11965–11984, https://doi.org/10.5194/acp-13-11965-2013, 2013.

Kärcher, B., Burkhardt, U., Unterstrasser, S., and Minnis, P.: Factors controlling contrail cirrus optical depth, Atmos Chem
485   Phys, 9, 6229–6254, https://doi.org/10.5194/acp-9-6229-2009, 2009.

Kärcher, B., Burkhardt, U., Ponater, M., and Fromming, C.: Importance of representing optical depth variability for estimates of global line-shaped contrail radiative forcing, Proc Natl Acad Sci U S A, 107, 19181–19184, https://doi.org/10.1073/pnas.1005555107 [doi], 2010.

Lee, D. S., Fahey, D. W., Skowron, A., Allen, M. R., Burkhardt, U., Chen, Q., Doherty, S. J., Freeman, S., Forster, P. M.,
490   Fuglestvedt, J., Gettelman, A., De León, R. R., Lim, L. L., Lund, M. T., Millar, R. J., Owen, B., Penner, J. E., Pitari, G., Prather, M. J., Sausen, R., and Wilcox, L. J.: The contribution of global aviation to anthropogenic climate forcing for 2000 to 2018, Atmos Environ, 244, 117834, https://doi.org/10.1016/J.ATMOSENV.2020.117834, 2021.

Lewellen, D. C.: Persistent contrails and contrail cirrus. Part II: Full lifetime behavior, J Atmos Sci, 71, 4420–4438, https://doi.org/10.1175/JAS-D-13-0317.1, 2014.

495   Lewellen, D. C. and Lewellen, W. S.: The Effects of Aircraft Wake Dynamics on Contrail Development, J Atmos Sci, 58, 390–406, https://doi.org/10.1175/1520-0469(2001)058<0390:TEOAWD>2.0.CO;2, 2001.

Lewellen, D. C., Meza, O., Huebsch, W. W., Lewellen, D. C., Meza, O., and Huebsch, W. W.: Persistent Contrails and Contrail Cirrus. Part I: Large-Eddy Simulations from Inception to Demise, J Atmos Sci, 71, 4399–4419, https://doi.org/10.1175/JAS-D-13-0316.1, 2014.

500   Long, C. N., Sabburg, J. M., Calbó, J., and Pagès, D.: Retrieving Cloud Characteristics from Ground-Based Daytime Color All-Sky Images, J Atmos Ocean Technol, 23, 633–652, https://doi.org/10.1175/JTECH1875.1, 2006.

Mannstein, H., Brömser, A., and Bugliaro, L.: Ground-based observations for the validation of contrails and cirrus detection in satellite imagery, Atmos Meas Tech, 3, 655–669, https://doi.org/10.5194/amt-3-655-2010, 2010.

Marjani, S., Tesche, M., Bräuer, P., Sourdeval, O., and Quaas, J.: Satellite Observations of the Impact of Individual Aircraft
505   on Ice Crystal Number in Thin Cirrus Clouds, Geophys Res Lett, 49, e2021GL096173, https://doi.org/10.1029/2021GL096173, 2022.

Meerkötter, R., Schumann, U., Doelling, D. R., Minnis, P., Nakajima, T., and Tsushima, Y.: Radiative forcing by contrails, Ann Geophys, 17, 1080–1094, https://doi.org/10.1007/s00585-999-1080-7, 1999.

Meijer, V. R., Kulik, L., Eastham, S. D., Allroggen, F., Speth, R. L., Karaman, S., and Barrett, S. R. H.: Contrail coverage
510   over the United States before and during the COVID-19 pandemic, Environmental Research Letters, 17, 034039, https://doi.org/10.1088/1748-9326/AC26F0, 2022.

Pedregosa, F., Varoquaux, G., Gramfort, A., Michel, V., Thirion, B., Grisel, O., Blondel, M., Prettenhofer, P., Weiss, R., Dubourg, V., Vanderplas, J., Passos, A., Cournapeau, D., Brucher, M., Perrot, M., and Duchesnay, É.: Scikit-learn: Machine Learning in Python, Journal of Machine Learning Research, 12, 2825–2830, https://arxiv.org/abs/1201.0490v4 (last access: 7 September 2023), 2012.

Petzold, A., Thouret, V., Gerbig, C., Zahn, A., Brenninkmeijer, C. A. M., Gallagher, M., Hermann, M., Pontaud, M., Ziereis, H., Boulanger, D., Marshall, J., NéDélec, P., Smit, H. G. J., Friess, U., Flaud, J. M., Wahner, A., Cammas, J. P., Volz-Thomas, A., Thomas, K., Rohs, S., Bundke, U., Neis, P., Berkes, F., Houben, N., Berg, M., Tappertzhofen, M., Blomel, T., Pätz, W., Filges, A., Boschetti, F., Verma, S., Baum, S., Athier, G., Cousin, J. M., Sauvage, B., Blot, R., Clark, H., Gaudel, A., Gressent, A., Auby, A., Fontaine, A., Gautron, B., Bennouna, Y., Petetin, H., Karcher, F., Abonnel, C., Dandin, P., Beswick, K., Wang, K. Y., Rauthe-Schöch, A., Baker, A. K., Riede, H., Gromov, S., Zimmermann, P., Thorenz, U., Scharffe, D., Koeppel, C., Slemr, F., Schuck, T. J., Umezawa, T., Ditas, J., Cheng, Y., Schneider, J., Williams, J., Neumaier, M., Christner, E., Fischbeck, G., Safadi, L., Petrelli, A., Gehrlein, T., Heger, S., Dyroff, C., Weber, S., Assmann, D., Rubach, F., Weigelt, A., Stratmann, G., Stock, P., Penth, L., Walter, D., Heue, K. P., Allouche, Y., Marizy, C., Hermira, J., Bringtown, S., Saueressig, G., Seidel, N., Huf, M., Waibel, A., Franke, H., Klaus, C., Stosius, R., Baumgardner, D., Braathen, G., Paulin, M., and Garnett, N.: Global-scale atmosphere monitoring by in-service aircraft – current achievements and future prospects of the European Research Infrastructure IAGOS, Tellus B Chem Phys Meteorol, 67, 1–24, https://doi.org/10.3402/TELLUSB.V67.28452, 2015.

Quaas, J., Gryspeerdt, E., Vautard, R., and Boucher, O.: Climate impact of aircraft-induced cirrus assessed from satellite observations before and during COVID-19, Environmental Research Letters, 16, 064051, https://doi.org/10.1088/1748-9326/ABF686, 2021.

Raspberry Pi: Accessories: Camera, https://www.raspberrypi.com/documentation/accessories/camera.html (last access: 16 August 2023), n.d.

Reutter, P., Neis, P., Rohs, S., and Sauvage, B.: Ice supersaturated regions: Properties and validation of ERA-Interim reanalysis with IAGOS in situ water vapour measurements, Atmos Chem Phys, 20, 787–804, https://doi.org/10.5194/ACP-20-787-2020, 2020.

Rosenow, J., Hospodka, J., Lán, S., and Fricke, H.: Validation of a Contrail Life-Cycle Model in Central Europe, Sustainability 2023, Vol. 15, Page 8669, 15, 8669, https://doi.org/10.3390/SU15118669, 2023.

Schumann, U.: On conditions for contrail formation from aircraft exhausts, Meteorologische Zeitschrift, 5, 4–23, https://doi.org/10.1127/metz/5/1996/4, 1996.

Schumann, U.: A contrail cirrus prediction model, Geosci Model Dev, 5, 543–580, https://doi.org/10.5194/gmd-5-543-2012, 2012.

Schumann, U., Graf, K., and Mannstein, H.: Potential to reduce the climate impact of aviation by flight level changes, in: 3rd AIAA Atmospheric Space Environments Conference, https://doi.org/10.2514/6.2011-3376, 2011.

Schumann, U., Hempel, R., Flentje, H., Garhammer, M., Graf, K., Kox, S., Lösslein, H., and Mayer, B.: Contrail study with ground-based cameras, Atmos Meas Tech, 6, 3597–3612, https://doi.org/10.5194/amt-6-3597-2013, 2013.

Schumann, U., Penner, J. E., Chen, Y., Zhou, C., and Graf, K.: Dehydration effects from contrails in a coupled contrail–climate model, Atmos Chem Phys, 15, 11179–11199, https://doi.org/10.5194/acp-15-11179-2015, 2015.

Schumann, U., Baumann, R., Baumgardner, D., Bedka, S., Duda, D., Freudenthaler, V., Gayet, J.-F., Heymsfield, A. J., Minnis, P., and Quante, M.: Properties of individual contrails: A compilation of observations and some comparisons, Atmos Chem
550 Phys, 17, 1–62, https://doi.org/10.5194/acp-17-403-2017., 2017.

Schumann, U., Poll, I., Teoh, R., Koelle, R., Spinielli, E., Molloy, J., Koudis, G. S., Baumann, R., Bugliaro, L., Stettler, M., and Voigt, C.: Air traffic and contrail changes over Europe during COVID-19: A model study, Atmos Chem Phys, 21, 7429–7450, https://doi.org/10.5194/ACP-21-7429-2021, 2021.

Segrin, M. S., Coakley, J. A., and Tahnk, W. R.: MODIS Observations of Ship Tracks in Summertime Stratus off the West
555 Coast of the United States, J Atmos Sci, 64, 4330–4345, https://doi.org/10.1175/2007JAS2308.1, 2007.

Seiz, G., Shields, J., Feister, U., Baltsavias, E. P., and Gruen, A.: Cloud mapping with ground-based photogrammetric cameras, https://doi.org/10.1080/01431160600641822, 28, 2001–2032, https://doi.org/10.1080/01431160600641822, 2007.

Shapiro, M., Engberg, Z., Teoh, R., and Dean, T.: pycontrails: Python library for modeling aviation climate impacts, Zenodo, https://doi.org/10.5281/zenodo.7776686, 2023.

560 Shields, J. E., Karr, M. E., Johnson, R. W., and Burden, A. R.: Day/night whole sky imagers for 24-h cloud and sky assessment: history and overview, Applied Optics, Vol. 52, Issue 8, pp. 1605-1616, 52, 1605–1616, https://doi.org/10.1364/AO.52.001605, 2013.

Teoh, R., Schumann, U., and Stettler, M. E. J.: Beyond Contrail Avoidance: Efficacy of Flight Altitude Changes to Minimise Contrail Climate Forcing, Aerospace, 7, 121, https://doi.org/10.3390/aerospace7090121, 2020a.

565 Teoh, R., Schumann, U., Majumdar, A., and Stettler, M. E. J.: Mitigating the Climate Forcing of Aircraft Contrails by Small-Scale Diversions and Technology Adoption, Environ Sci Technol, 54, 2941–2950, https://doi.org/10.1021/acs.est.9b05608, 2020b.

Teoh, R., Schumann, U., Gryspeerdt, E., Shapiro, M., Molloy, J., Koudis, G., Voigt, C., and Stettler, M.: Aviation Contrail Climate Effects in the North Atlantic from 2016-2021., Atmos. Chem. Phys., 22, 10919–10935,
570 https://doi.org/https://doi.org/10.5194/acp-2022-169, 2022a.

Teoh, R., Schumann, U., Voigt, C., Schripp, T., Shapiro, M., Engberg, Z., Molloy, J., Koudis, G., and Stettler, M. E. J.: Targeted Use of Sustainable Aviation Fuel to Maximise Climate Benefits, Environ Sci Technol, 56, 17246–17255, https://doi.org/https://doi.org/10.1021/acs.est.2c05781, 2022b.

Teoh, R., Engberg, Z., Schumann, U., Voigt, C., Shapiro, M., Rohs, S., and Stettler, M. E. J.: Global aviation contrail climate
575 effects from 2019 to 2021 [preprint], EGUsphere, https://doi.org/https://doi.org/10.5194/egusphere-2023-1859, 2023.

Teoh, R., Engberg, Z., Shapiro, M., Dray, L., and Stettler, M. E. J.: The high-resolution Global Aviation emissions Inventory based on ADS-B (GAIA) for 2019–2021, Atmos Chem Phys, 24, 725–744, https://doi.org/10.5194/ACP-24-725-2024, 2024.

Tesche, M., Achtert, P., Glantz, P., and Noone, K. J.: Aviation effects on already-existing cirrus clouds, Nat Commun, 7, 1–6, https://doi.org/10.1038/ncomms12016, 2016.

580   Tsai, R. Y.: A Versatile Camera Calibration Technique for High-Accuracy 3D Machine Vision Metrology Using Off-the-Shelf TV Cameras and Lenses, IEEE Journal on Robotics and Automation, 3, 323–344, https://doi.org/10.1109/JRA.1987.1087109, 1987.

Unterstrasser, S.: Properties of young contrails: a parametrisation based on large-eddy simulations, Atmos Chem Phys, 16, 2059–2082, https://doi.org/10.5194/acp-16-2059-2016, 2016.

585   Vázquez-Navarro, M., Mannstein, H., and Kox, S.: Contrail life cycle and properties from 1 year of MSG/SEVIRI rapid-scan images, Atmos Chem Phys, 15, 8739–8749, https://doi.org/10.5194/acp-15-8739-2015, 2015.

World Meteorological Organization: International Cloud Atlas: Aircraft condensation trails, https://cloudatlas.wmo.int/en/aircraft-condensation-trails.html (last access: 13 May 2023), 2017.

Wu, Y., Jiang, S., Xu, Z., Zhu, S., and Cao, D.: Lens distortion correction based on one chessboard pattern image, Frontiers of
590   Optoelectronics, 8, 319–328, https://doi.org/10.1007/S12200-015-0453-7/METRICS, 2015.